nature geoscience

Article

https://doi.org/10.1038/s41561-023-01319-8

Radiative forcing from aerosol–cloud interactions enhanced by large-scale circulation adjustments

In the format provided by the authors and unedited

Content:

Sec. S1: Coupling of circulation and clouds in the tropical Pacific

To demonstrate the coupling between the large-scale circulation and cloud radiative effect in the tropical Pacific Ocean we use two independent data sets. To evaluate the strength of the circulation we use Sea Level Pressure (SLP) data form ICOADS (Freeman et al., 2017) (provided by the NOAA PSL at https://psl.noaa.gov), which is based on observations of surface marine data from various observing systems, including ships, buoys, meteorological coastal stations and tide gauges. As a measure of the tropical Pacific Walker circulations strength, we follow (L'Heureux et al., 2013) and use the SLP difference between the east (130°–80° W, 10° S–10° N) and west (110°–160° E, 10° S–10° N) tropical Pacific (ΔSLP_{pac}). To evaluate the cloud radiative effect (CRE) in the east Pacific cold pool (CRE CP*;* again defined as the 130°–80° W, 10° S–10° N box) we use CERES data (Wielicki et al., 1998) (available at: https://ceres.larc.nasa.gov/data/).

For both data sets we use the monthly-mean data over 23 years 2000-2022. Figure S1 demonstrates a positive correlation between ΔSLP_{pac} and CRE CP ($R=0.52$, p-value<0.01) suggesting that stronger Walker circulation (more negative ΔSLP_{pac}) is associate with stronger (in absolute values) CRE at the subsiding region, in line with previous work (Wood, 2012). Examining the correlation between ΔSLP_{pac} and CRE CP on a seasonal mean, rather than a monthly mean (Fig. S2) slightly increases the correlation ($R=0.6$, p-value<0.01).

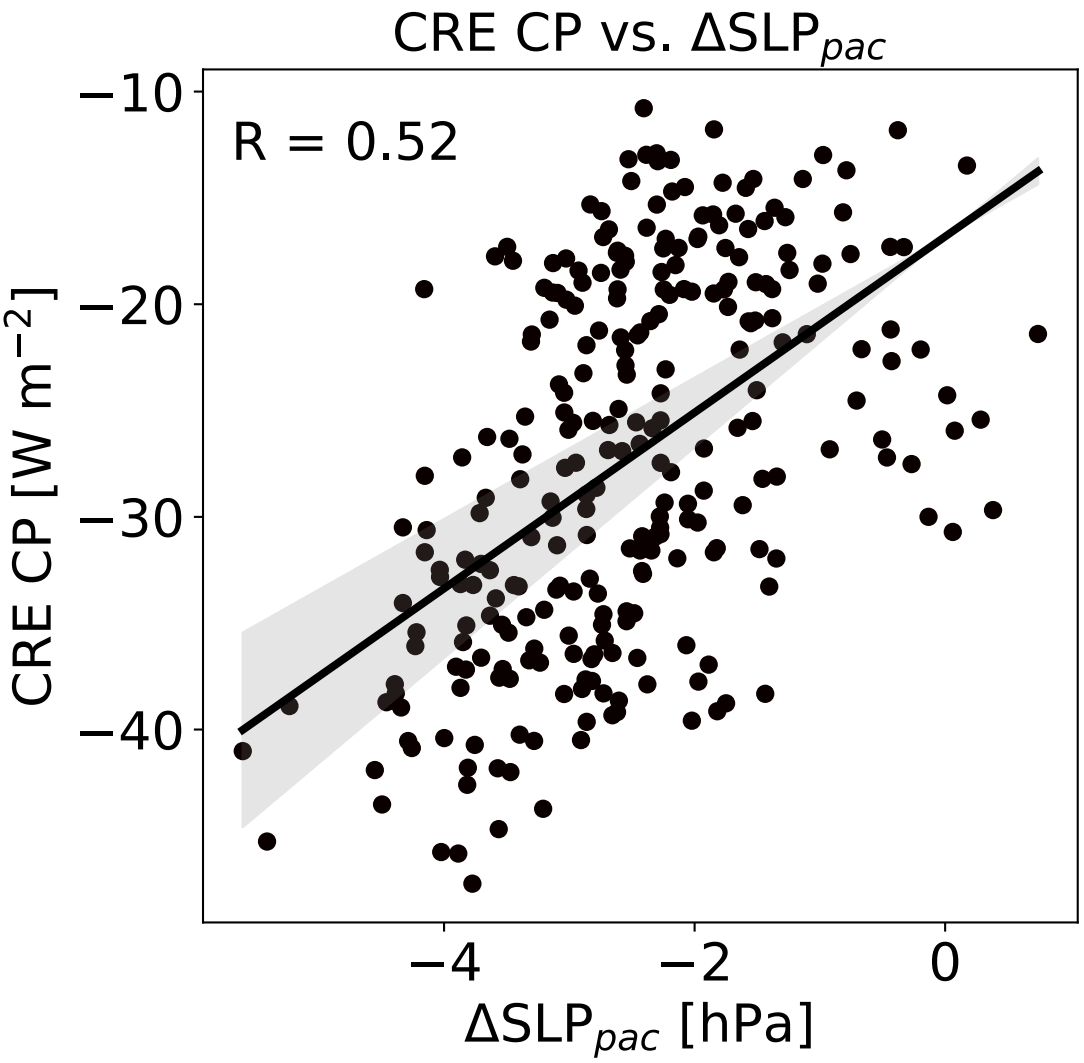

Figure S1. ΔSLP_{pac} vs. CRE CP for 23-years monthly mean observations.

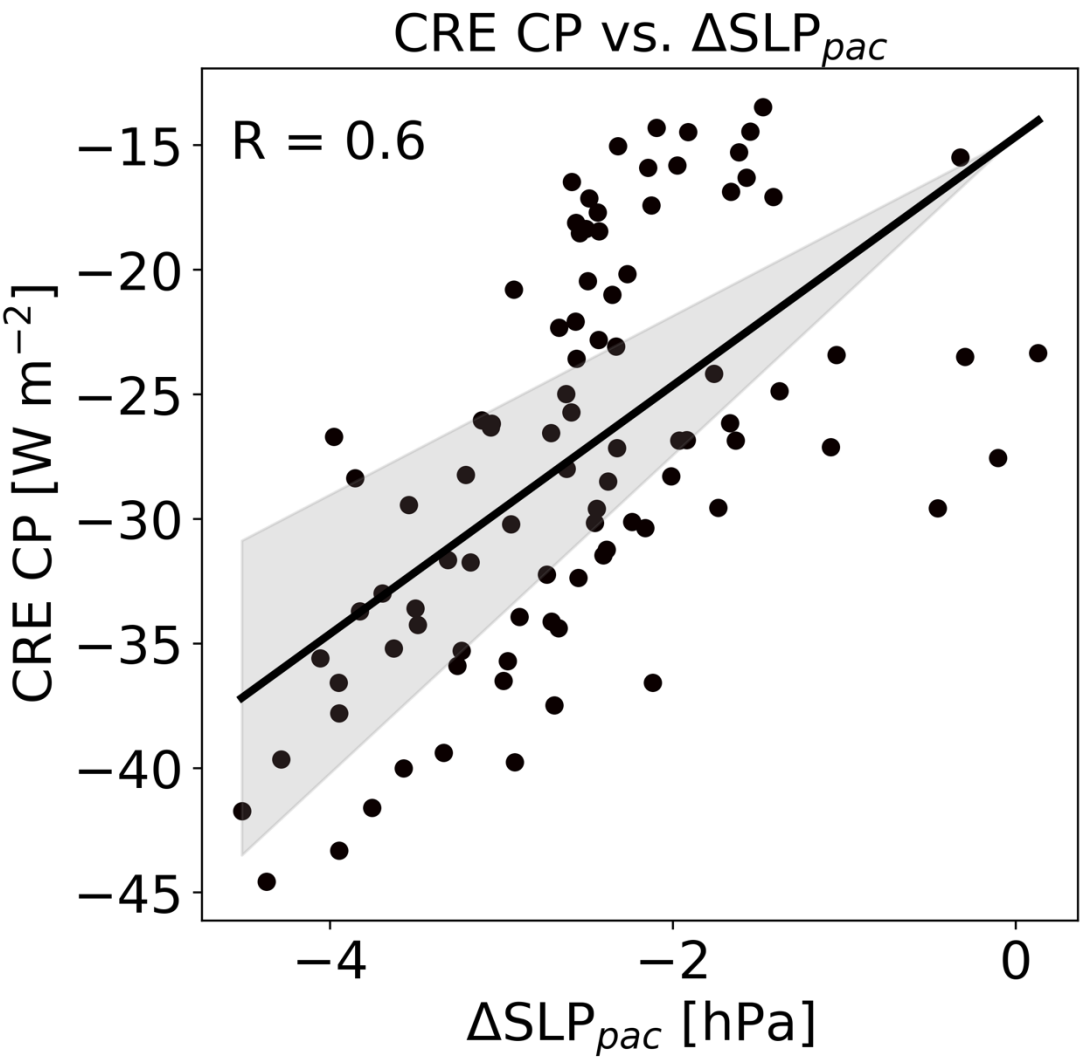

Figure S2. Same as Fig. S1 but for the seasonal mean rather than monthly mean.

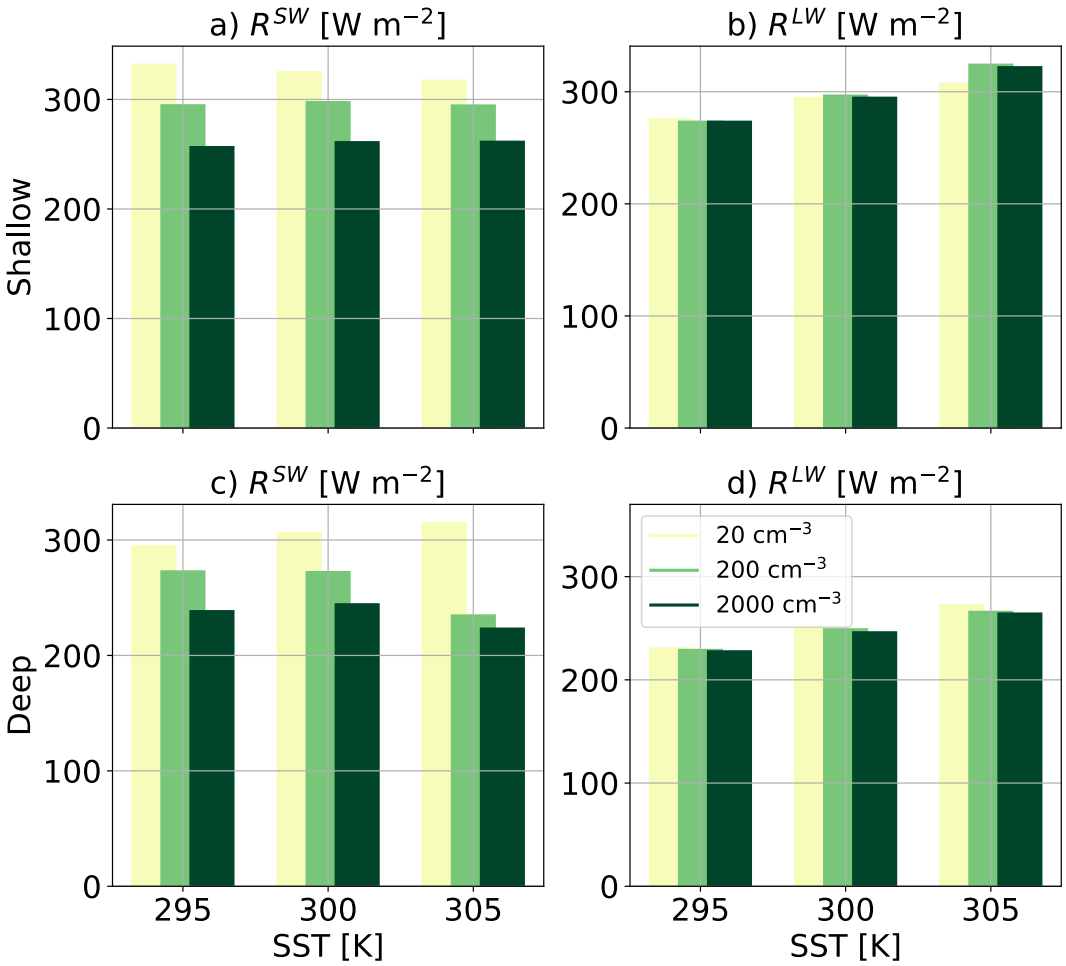

Figure S3. Time and spatial mean: net top-of-atmosphere energy gain in the shortwave (R^{SW} – a and c) and in the longwave (R^{LW} – b and d), for the different mock-Walker simulations conducted under different SST and aerosol concentration, and for the shallow (a – b) and deep regime (c – d) separately.

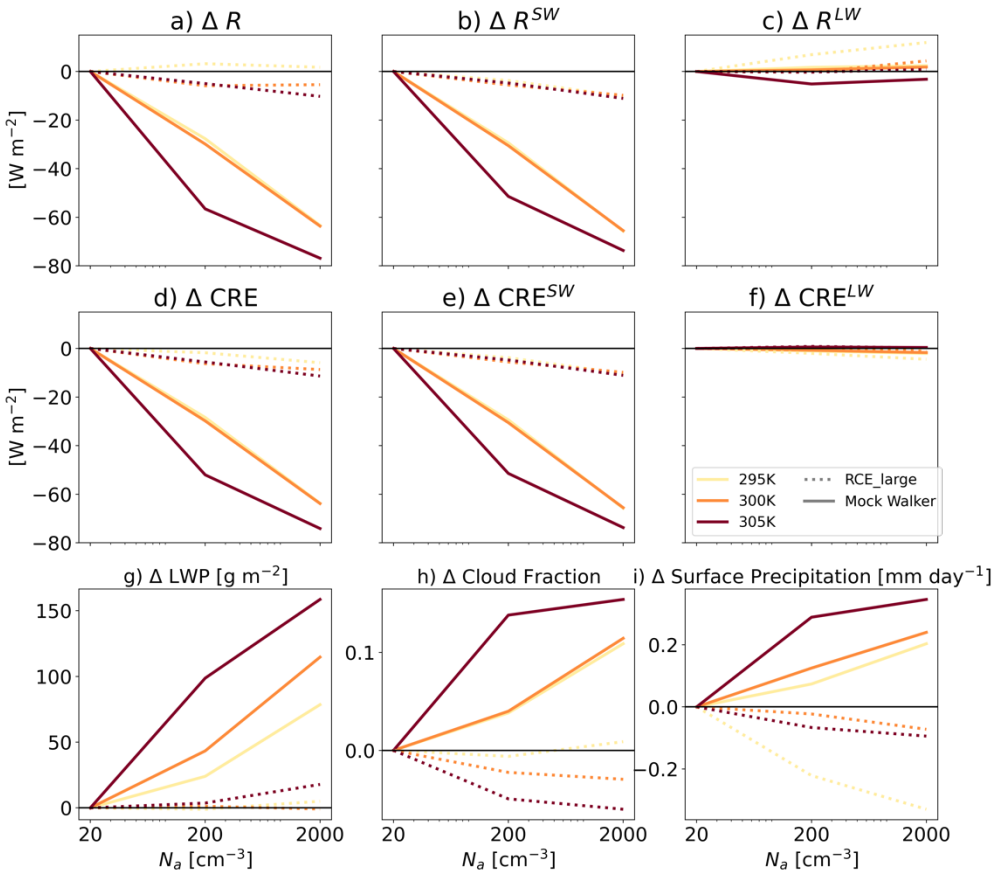

Figure S4. The change in the net top-of-atmosphere energy gain (ΔR) in total (shortwave + longwave) (a), in the shortwave (b) and in the longwave (c). The change in the cloud radiative effect (CRE) in total (shortwave + longwave) (d) in the shortwave (e) and in the longwave (f). The change in the domain mean liquid water path (LWP) (g), cloud fraction (h), and surface precipitation (i) due to a change in aerosol concentration – N_a (compared to the cleanest case – 20 cm^{-3}), for the different SSTs (indicated by different curves).

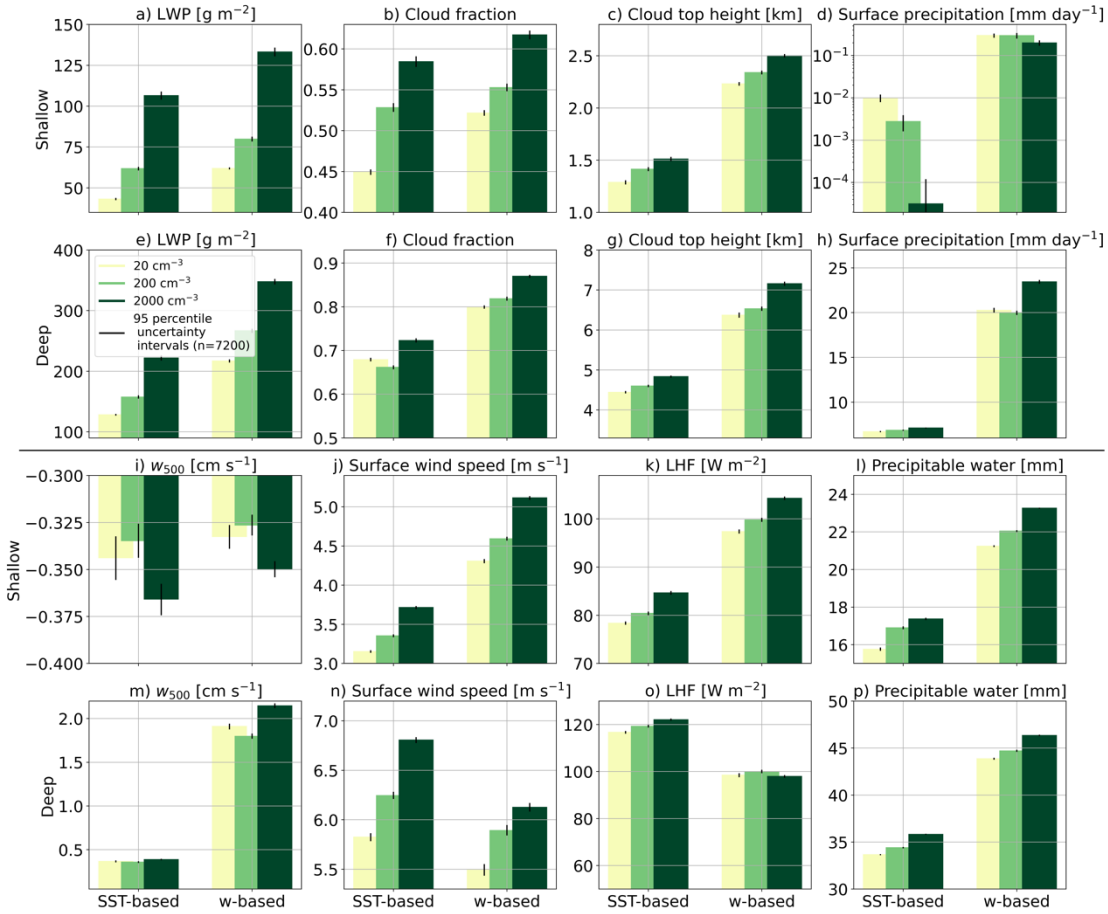

Figure S5. Time and spatial mean: liquid water path (LWP – a and e), cloud fraction (b and f), cloud top height (c and g), surface precipitation (d and h), large-scale vertical velocity at 500hPa (w500 – i and m), near surface wind speed (j and n), surface latent heat flux (LHF – k and o), and precipitable water (l and p) for the different mock-Walker simulations conducted under SST = 295K and different aerosol concentration, and for the shallow (a-d and i-l) and deep regime (e - h and m-p) separately, using two different methods for the separation (see main text for details). The bars represent the mean values, while the black vertical lines represent the 95 percentile uncertainty intervals (n=7200). Please note the logarithmic scale in the y-axis of (d).

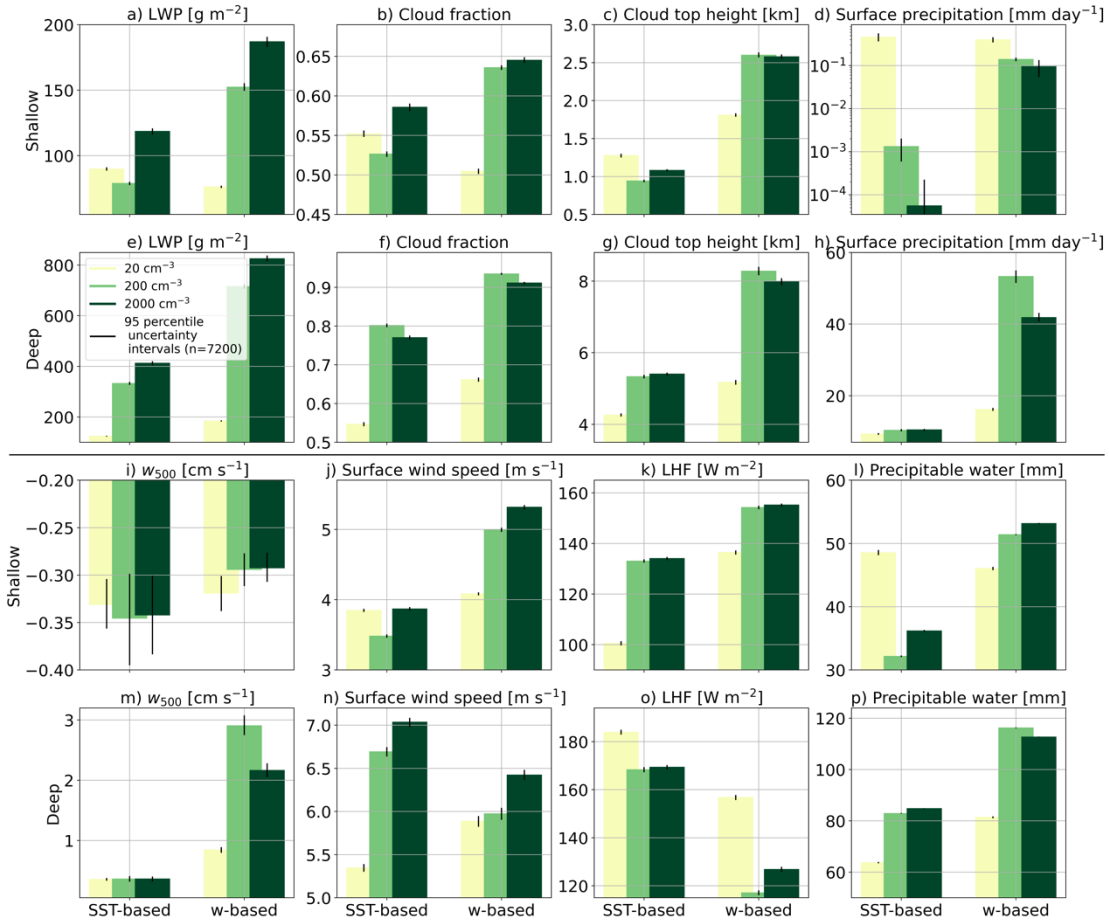

Figure S6. Time and spatial mean: liquid water path (LWP – a and e), cloud fraction (b and f), cloud top height (c and g), surface precipitation (d and h), large-scale vertical velocity at 500hPa (w500 – i and m), near surface wind speed (j and n), surface latent heat flux (LHF – k and o), and precipitable water (l and p) for the different mock-Walker simulations conducted under SST = 305K and different aerosol concentration, and for the shallow (a-d and i-l) and deep regime (e - h and m-p) separately, using two different methods for the separation (see main text for details). The bars represent the mean values, while the black vertical lines represent the 95 percentile uncertainty intervals (n=7200). Please note the logarithmic scale in the y-axis of (d).

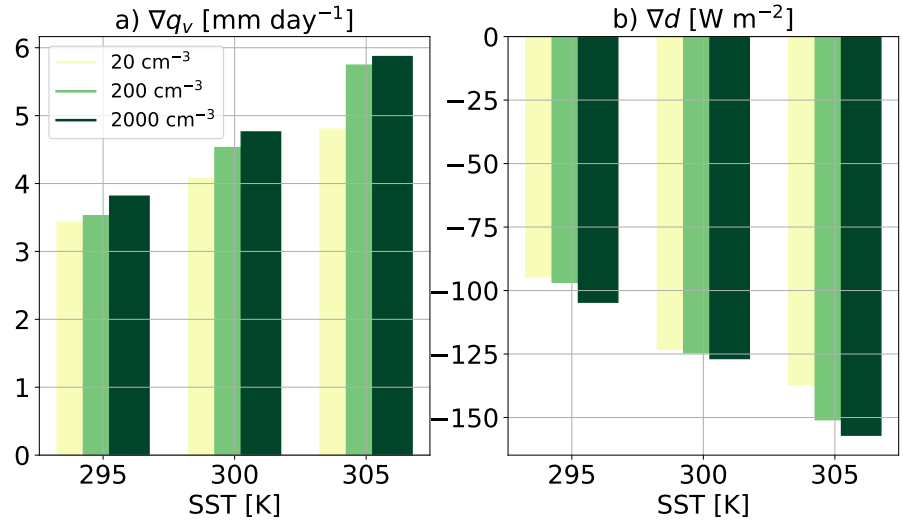

Figure S7. Mean divergence out of the shallow regime of: water vapor (∇q_v – a), and dry static energy (∇d – b) for the different mock-Walker simulations conducted under different SST and aerosol concentration. This Figure is similar to Fig. 4 in the main text by uses w_{500} instead of SST to separate the different cloud regimes.

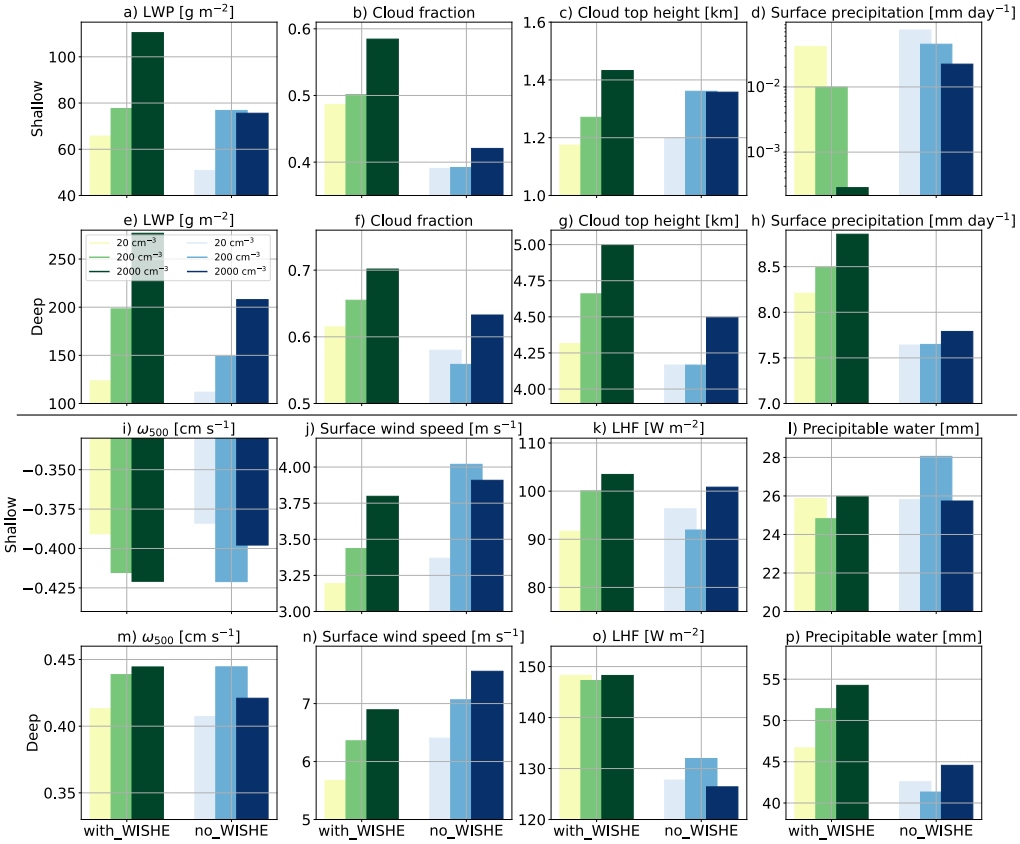

Figure S8. Time and spatial mean: liquid water path (LWP – a and e), cloud fraction (b and f), cloud top height (c and g), surface precipitation (d and h), large-scale vertical velocity at 500hPa (w_{500} – i and m), near surface wind speed (j and n), surface latent heat flux (LHF – k and o), and precipitable water (l and p) for the different mock-Walker simulations conducted under SST = 300K and different aerosol concentration, for the shallow (a – d and i – l) and deep regime (e – h and m – p) separately and for the regular simulations which include the WISHE feedback (with_WISHE) and the simulations that exclude it (no_WISHE). Please note the logarithmic scale in the y-axis of (d).

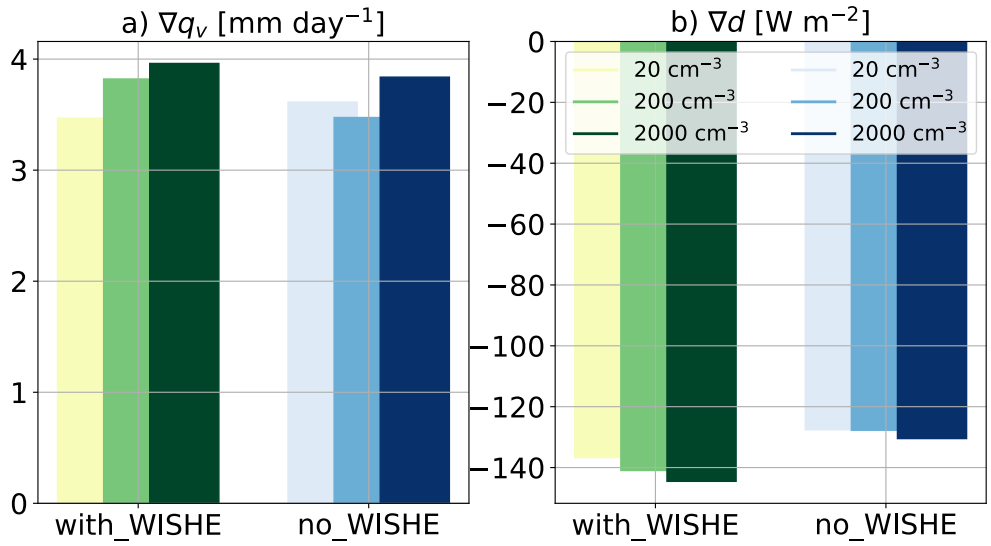

Figure S9. Mean divergence out of the shallow regime of: water vapor (∇q_v – a), and dry static energy (∇d – b) for the different mock-Walker simulations conducted under SST = 300K and different aerosol concentration for the regular simulations which include the WISHE feedback (with_WISHE) and the simulations which exclude it (no_WISHE).

Sec. S2: The relative role of shallow-convection and deep-convection pollution

To examine the relative role of aerosol perturbations in the shallow and deep portion of the domain on the large-scale circulation adjustment we have conducted 6 additional simulations in which N_a is either concentrated in the high or low SST region (Fig. S10; Methods). This set of simulations suggests that indeed addition of aerosol to the shallow dominated regime plays a larger role than addition of the same amount of aerosols to the deep regime (Figs. S11-12). Specifically, it demonstrates that increasing N_a in the shallow dominated part of the domain, suppresses the rainfall in this part, enhances the surface evaporation, and hence increases (decreases) the water vapor (dry static energy) advection out of the shallow regime. The increased water vapor advection into the deep part when only the shallow part is polluted results in increase in precipitation in the deep part. The stronger deep convective precipitation in the case of shallow concentrated pollution compared with deep concentrated pollution suggests that it is not local convective invigoration by aerosols that drive the trend seen in our original simulations but rather the rain suppression in the shallow part. Hence, this set of simulations supports our original hypothesis.

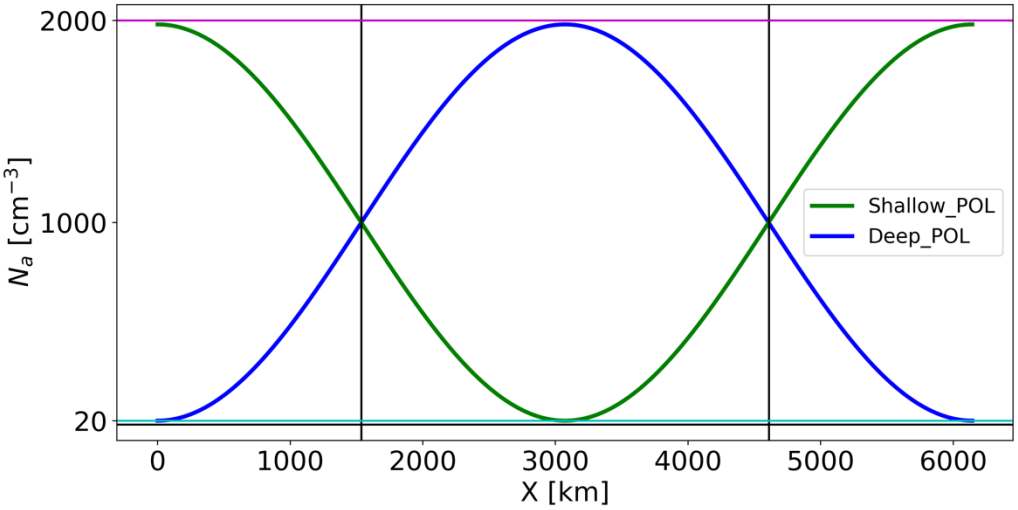

Figure S10. The N_a spatial distribution used in the non-spatially uniform N_a simulations.

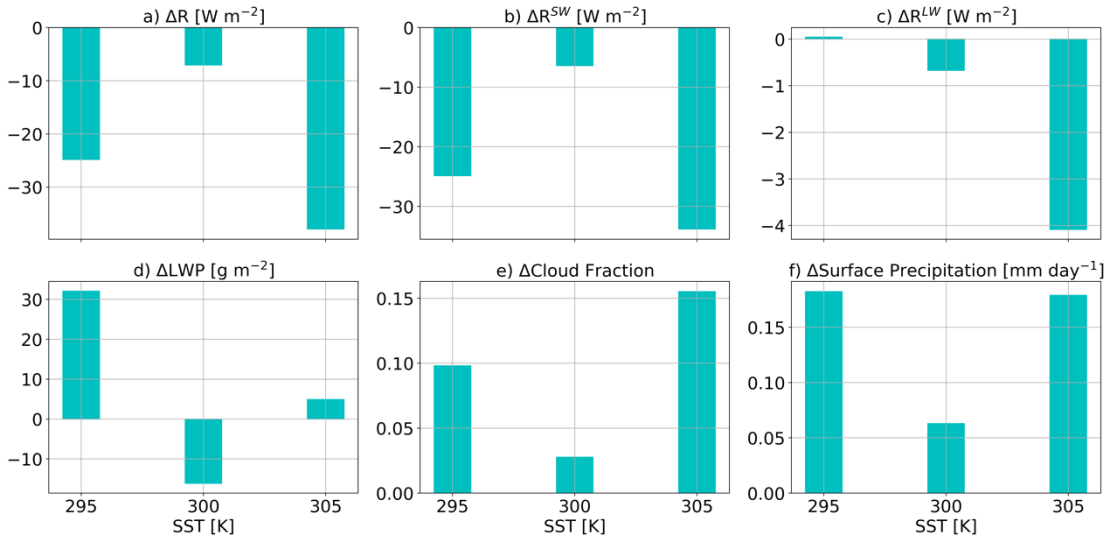

Figure S11. The domain- and time-mean difference in the non-spatially uniform N_a simulations between Shallow_POL and Deep_POL: net top-of-atmosphere energy gain (ΔR) in total (shortwave + longwave); a), in the shortwave (b) and in the longwave (c), and the change in the domain-mean liquid water path (LWP; g), cloud fraction (h), and surface precipitation (i) for the different mock-Walker simulations conducted under different SSTs.

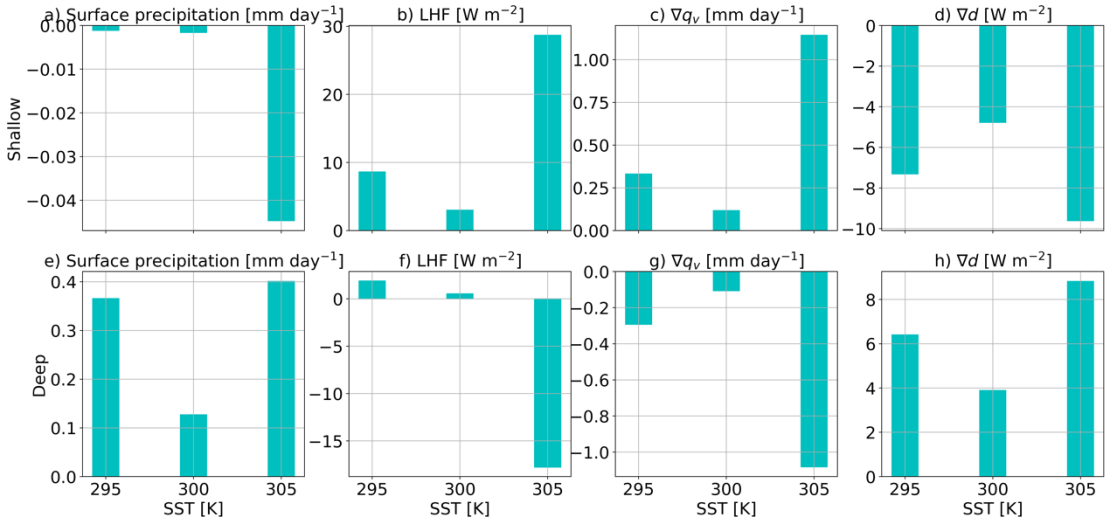

Figure S12. The domain- and time-mean difference in the non-spatially uniform N_a simulations between Shallow_POL and Deep_POL: surface precipitation (a and e), surface latent heat flux (LHF – b and f), and, divergence of: water vapor (∇q_v – c and g), and dry static energy (∇d – d and h) for the different mock-Walker simulations conducted under different SSTs, and for the shallow (a-d) and deep regime (e - h) separately using the SST-based separation (see main text for details).

Sec. S3: Transient simulations

In this paper we are focusing on ``adjustments" to ACI, i.e., under a fixed SST framework. To verify the suitability of this separation in our work, we need to make sure that the time required for the large-scale circulation adjustments to form is short compared to the time required for the SST to significantly react to the initial radiative forcing (on the order of a few years). In addition, we would like to separately estimate the relative importance of cloud adjustments from local ACI and cloud adjustments from large-scale circulation changes. To do that, we have conducted four additional transient simulations branching-off the mock Walker simulation at different times, thus initiated with different initial conditions (Methods).

Figure S13, demonstrates that during the first 20-days of the simulations the ensemble-mean near surface wind speed difference is close to zero suggesting that the large-scale circulation hasn't reacted yet. During this time, the LWP and CF responses are fairly small suggesting weak cloud adjustments due to local ACI. During this period the change in R^{SW} is relatively small and dominated by the Twomey effect. After about 30 days of simulation, the ensemble-mean difference in the near surface wind speed stabilizes at around the difference seen in the original runs (Fig. 3 in the main text) During this later period the LWP and CF responses increases and stabilized at around the difference seen in the original runs (Fig. 2 in the main text), which drive an increase also in the R^{SW} response that also stabilized at around the difference seen in the original runs (Fig. 2 in the main text). The R^{SW} response is much weaker, consistent with our original results.

These results suggest that the vast majority of the cloud adjustments (the LWP and CF responses), and hence also a large fraction of the R^{SW} response, are driven by large-scale circulation adjustments, rather than by local, faster reacting, adjustments. In addition, it demonstrates that the large-scale circulations adjustments occur on time scale (~month) shorter than the time required for significant SST changes (years).

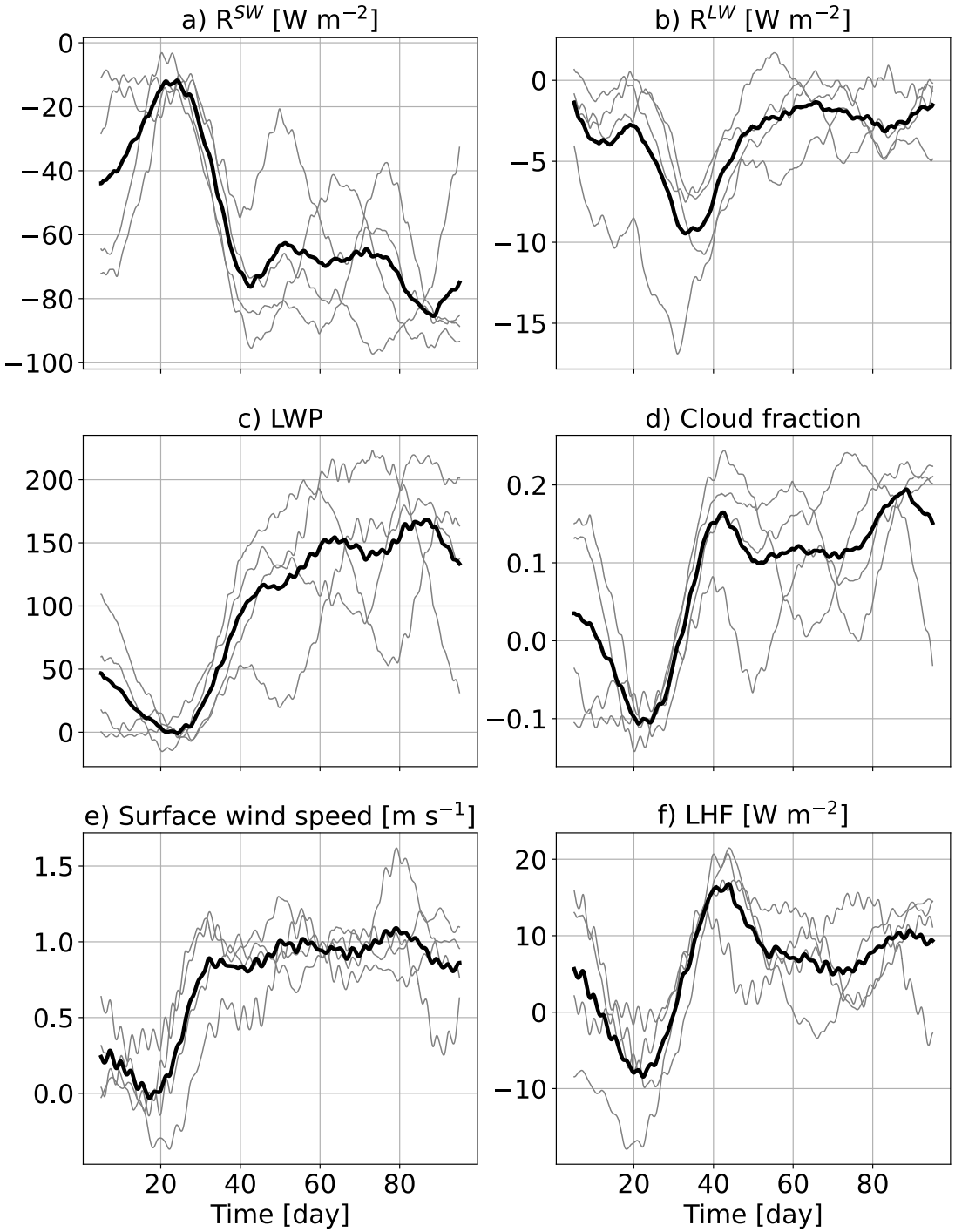

Figure S13. The response of (a) R^{SW}, (b) R^{LW}, (c) LWP, (d) cloud fraction, (e) near surface wind speed, and (f) surface latent heat flux (LHF) to an increase in N_a along time of 100-day long transient simulations. The four different ensemble members (presented in gray) were initiated under different initial conditions using the conditions at different times (after 100, 200, 300 and 400 days) from the baseline simulations (SST = 300 K and N_a = 20 cm^{-3}). These transient simulations were conducted with higher N_a of 2000 cm^{-3}. This Figure presents the time evolution of

the domain-mean difference of these simulations from the time-mean of the baseline simulation. The ensemble mean is presented in black.

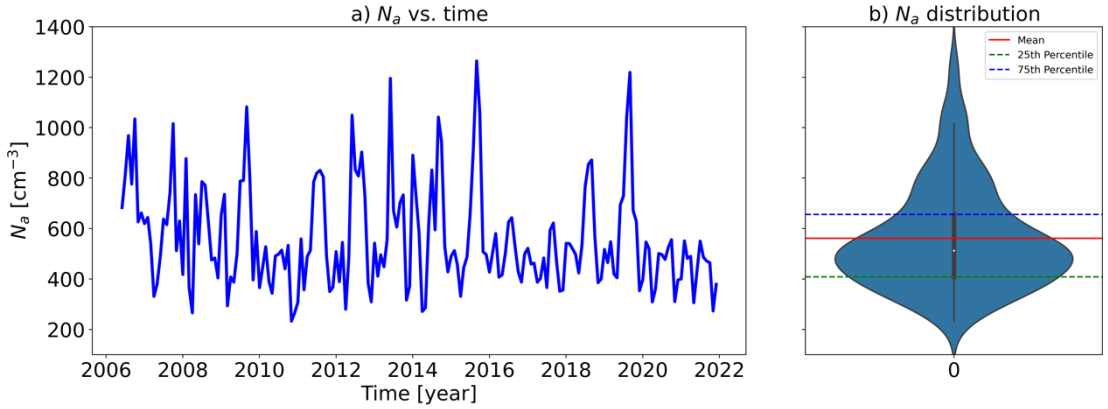

Figure S14. Observational-based estimations of the variability of the monthly-mean N_a concentrations (evaluated at 0.2% super saturation) at the boundary layer (height of 500m above sea level) over the Eastern tropical Pacific (130°–80° W, 10° S–10° N). a) time evolution of the area-average N_a concentration along 15.5 years, and b) the distribution of the area-average N_a concentration (n=186).

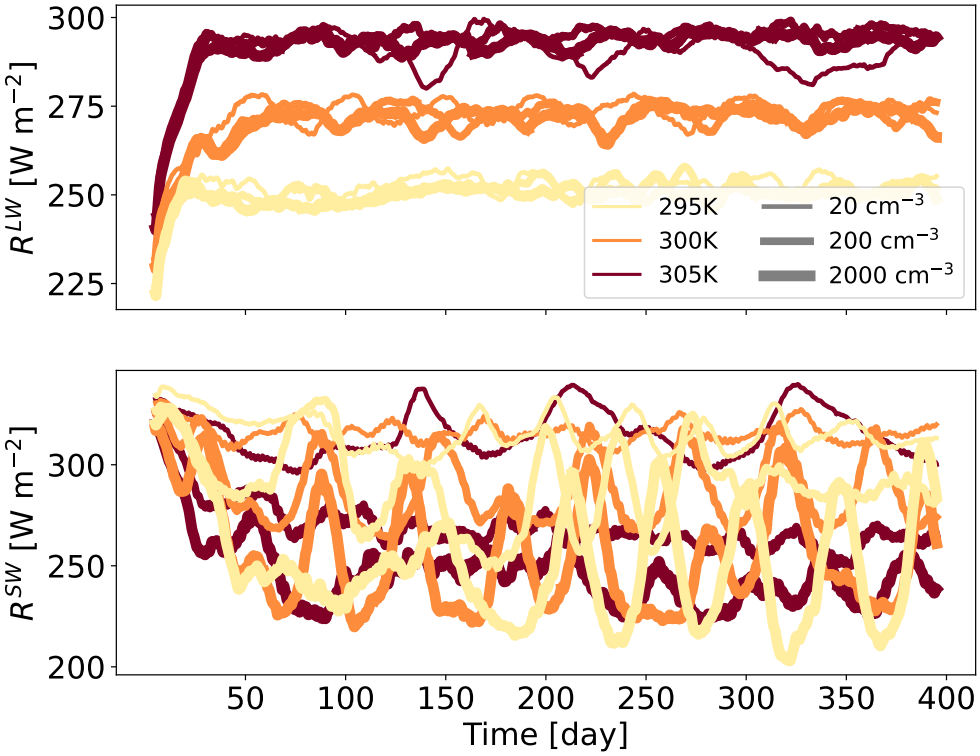

Figure S15. 10-day running mean top-of-atmosphere energy net longwave (a – R^{LW}), and shortwave (b – R^{SW}) radiative flux as a function of time for the different mock-Walker simulations conducted under different SST and aerosol concentration.

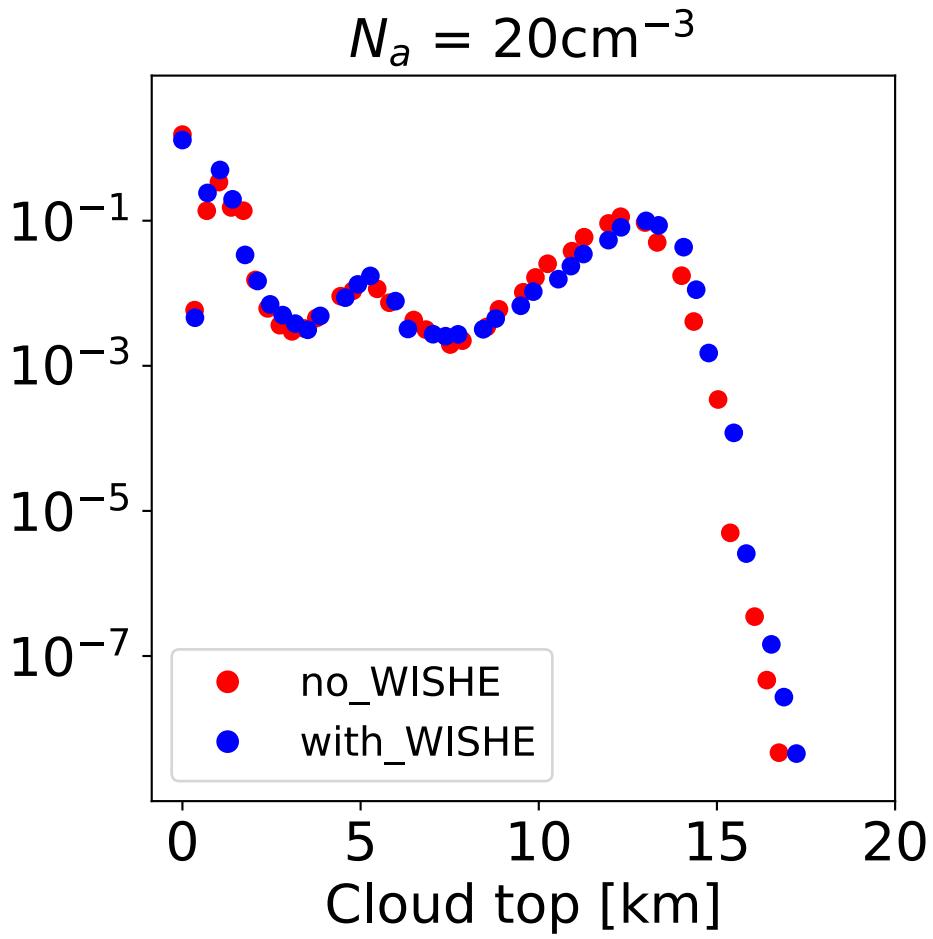

Figure S16. Histograms of the cloud top height in the mock-Walker simulations conducted under SST = 300K and N_a = 20 cm^{-3} for the regular simulations which include the WISHE feedback (with_WISHE) and the simulations which exclude it (no_WISHE).

References

Freeman, E., Woodruff, S. D., Worley, S. J., Lubker, S. J., Kent, E. C., Angel, W. E., Berry, D. I., Brohan, P., Eastman, R., and Gates, L.: ICOADS Release 3.0: a major update to the historical marine climate record, International Journal of Climatology, 37, 2211-2232, 2017.

L'Heureux, M. L., Lee, S., and Lyon, B.: Recent multidecadal strengthening of the Walker circulation across the tropical Pacific, Nature Climate Change, 3, 571-576, 2013.

Wielicki, B. A., Barkstrom, B. R., Baum, B. A., Charlock, T. P., Green, R. N., Kratz, D. P., Lee, R. B., Minnis, P., Smith, G. L., and Wong, T.: Clouds and the Earth's Radiant Energy System (CERES): algorithm overview, Geoscience and Remote Sensing, IEEE Transactions on, 36, 1127-1141, 1998.

Wood, R.: Stratocumulus clouds, Monthly Weather Review, 140, 2373-2423, 2012.